JOURNAL OF AIRCRAFT
Vol. 48, No. 1, January–February 2011

Computational Investigation of Flow Around a Parachute Model

Mark McQuilling,* Lauren Lobosky,† and Steven Sander†
Saint Louis University, St. Louis, Missouri 63103

DOI: 10.2514/1.46255

Studying airdrop system aerodynamics is very challenging due to the coupling of aerodynamic forces and structural dynamics. Simplified models not containing the dynamic system coupling can yield information useful for fundamental understanding and advanced code validation. This paper presents steady-state results from a Reynolds-averaged Navier–Stokes flow solver simulating flow around a parachute model at a Reynolds number of 365,000 over five pitch angles of 0, −5, −8, −10, and −12°. The parachute model, rigid and hemispherical in shape, is similar to that of a ribbon parachute with four ribbons or rings. Pressure results are compared with experimental data to judge accuracy of the simulations. Additional results include pressure and vorticity contours, as well as computational oil-flow visualizations. These results illustrate the complex flow pattern in and around the ribbon parachute model, and they elaborate on existing data available for fluid–structure interaction code development.

Nomenclature

C_p = pressure coefficient, $(p - p_\infty)/(0.5\rho u_\infty^2)$
d = skirt diameter
K_p = static pressure parameter, $(p_{\text{inside}} - p_{\text{outside}})/(0.5\rho u_\infty^2)$
p = static pressure
p_∞ = average static pressure at inlet plane
Re = Reynolds number, $(\rho U d)/\mu$
u = streamwise velocity
v = cross-stream vertical velocity
w = cross stream in and out of page velocity
α = pitch angle
ζ = vorticity magnitude, $\sqrt{(\partial w/\partial y - \partial v/\partial z)^2 + (\partial u/\partial z - \partial w/\partial x)^2 + (\partial v/\partial x - \partial u/\partial y)^2}$
μ = viscosity of water
ρ = fluid density
ϕ = roll angle

Introduction

THE development and validation of advanced computational modeling strategies that couple fluid and structural solvers for airdrop applications has recently been targeted as a major item of worldwide importance [1]. This collaborative group of subject-matter experts from France, Germany, the United Kingdom, and the United States also identified the development of high-quality validation cases related to parachute geometries as a vital step in the advancement of fluid–structure interaction (FSI) capability. Airdrop system aerodynamics contain a high degree of unsteady phenomena [2], including six-degree-of-freedom translations and rotations, separated flows, bluff body vortex shedding, forebody influence on downstream parachute geometries, and the time-dependent structural changes of highly flexible and lightweight structures that are coupled to the unsteady flow phenomena.

Presented as Paper 2009-3978 at the 19th AIAA Computational Fluid Dynamics, San Antonio, TX, 22–25 June 2009; received 17 October 2009; revision received 22 October 2010; accepted for publication 25 October 2010.

*Assistant Professor, Aerospace and Mechanical Engineering, Parks College of Engineering, Aviation, and Technology, Center for Fluids at All Scales, 3450 Lindell Boulevard. Member AIAA.

†Undergraduate Student, Aerospace Engineering, Parks College of Engineering, Aviation, and Technology, Center for Fluids at All Scales, 3450 Lindell Boulevard. Student Member AIAA.

Generating high-quality validation data can be a difficult process, especially on parachute geometries containing the coupling of physics mentioned previously. AIAA recognizes validation as "the degree to which a model is an accurate representation of the real world from the perspective of the intended uses of the model" [3]. Seeger et al. also noted the complexity of FSI development related to airdrop applications and further suggested a stepwise approach toward the validation of potential FSI codes that included comparisons of FSI codes to experimental data and other standard computational fluid dynamics (CFD) simulations on rigid geometries, as well as CFD-to-CFD code comparisons based on well-defined geometries with high-quality experimental data [1].

To provide high-quality validation experiments intended for code development, McBride et al. instrumented a rigid and porous ribbon parachute model with pressure taps and translated the model at a time-dependent velocity history in a water tunnel [4]. These experiments measured the static pressure at various locations along the inside and outside of the ribbons at three model pitch angles, and each test condition was repeated multiple times in order to provide an extensive uncertainty quantification. Static pressure was measured instead of an integrated quantity such as drag in order to provide information on the fundamental fluid forces occurring around a complex geometry. Although McBride et al. provided the high-quality static pressure results on a geometry containing relevant fluid dynamic phenomena, there was no determination of relevant flow physics including flowfield descriptions, surface forces, and flow separations and reattachments. These details are necessary to ensure developing codes can accurately predict the salient features of parachute flowfields.

The current study simulates the steady-state flow around the same geometry, as described by McBride et al. [4], using a Reynolds-averaged Navier–Stokes (RANS) flow solver. The model is generated in a CAD software before it is imported into the CFD program, where it is subjected to an incoming flow of water at 1.2192 m/s, producing a Reynolds number of 365,000. To provide the critical flow details necessary to understand the complex flow around the ribbon parachute model, results include pressure and vorticity contours along with surface oil-flow visualizations and integrated surface forces.

Computational Details

The steady-state RANS equations were solved using the SC/Tetra CFD software. SC/Tetra is a finite volume flow solver using the SIMPLEC [5] method and MUSCL [6] differentiation technique for solving the RANS equations. The current implementation employs second-order accuracy in space and first-order accuracy in time. SC/Tetra employs an unstructured tetrahedral mesh [7] using prism elements to resolve boundary layers, and it contains all preprocessing

and postprocessing required for CFD analysis. In this work, the k-ϵ turbulence model was used for turbulence closure. The computational domain length extended 6.56 ft (2 m) upstream of the skirt and 19.69 ft (6 m) downstream of the model support; these distances were judged sufficient by increasing them until the total drag and lift forces on the model did not appreciably change. The domain height of 10 ft (3.05 m) and width of 14 ft (4.27 m) matched the water-tunnel dimensions of the experiments [4] and, as such, were deemed necessary in the simulations to include the pressure influences of these physical boundaries surrounding the model. Boundary conditions included the no-slip condition on all ribbons and support structures, an inlet velocity of 1.2192 m/s of water at the upstream face, a downstream boundary of zero static pressure, and all remaining sides of the domain prescribed as free-slip surfaces. The gravity body force was also applied as -9.81 m/s^2 in the y direction. All computations were executed on a single PC with a dual-core 3.2 GHz processor and 8 GB of memory; typical run times for each simulation were on the order of 3.5 days, where convergence was determined after the relative residuals decreased by four orders of magnitude.

Model Geometry

The ribbon parachute model geometry was created in a three-dimensional modeling program using descriptions provided by McBride et al. [4]. In these experiments, the model instrumented with pressure taps was placed in a water tunnel and translated at a time-dependent velocity history. The model was a 12-in. (0.3048 m)-diam hemispherical shape comprising four rigid 1.75 in. (0.04445 m) arc-length ribbons with a ribbon-to-slot-width ratio of four, leaving a vent in the center. This model can be seen in Fig. 1, which includes a close-up of the parachute along with ribbon numbers and coordinate axes for the $-10°$ pitch case. Thus, the x direction corresponds to the freestream direction for all pitch angles. Each ribbon is $\frac{3}{32}$ in. (2.38e − 3 m) thick and fully rounded on the leading and trailing edges. The ribbons are supported by four evenly spaced, 0.25-in. (6.35e − 2 m)-thick struts that connect to a 1-in. (0.0254 m)-diam sting. The large struts and sting apparatus were necessary in the experiments in order to house pressure tubing for the taps located on the ribbons and are therefore included in the simulations. These pressure taps were placed on the inner and outer surfaces at five equally spaced locations across the widths of the ribbons. Additional taps were also located across the hemisphere in order to judge flow symmetry about the central axis. The experimental model was twisted between runs to provide pressure data at several locations around the hemisphere, which included roll angles of 0, 45, 90, 135, and 180° relative to the bottom of the model and judged positive clockwise when viewing the model from the front. Experimental results were obtained at pitch angles of -0, -5, and $-10°$ (judged negative counterclockwise from negative x direction). The velocity time history chosen for the experiments translated the model with linear acceleration from rest at 2 ft/s^2 (0.6096 m/s^2) for 2 s, then constant velocity of 4 ft/s (1.2192 m/s) for a period of 6 s, then linear deceleration at -2 ft/s^2 (-0.6096 m/s^2) until rest, after which data was collected for another 8 s. In this study, only the constant velocity portion of the trajectory is simulated, and results were obtained at five pitch angles of 0, -5, -8, -10, and $-12°$. The results at -8 and $-12°$ were simulated in order to look for additional occurrences of the two modes seen in the experimental pressure results at a $-10°$ pitch and 45° roll angle.

Mesh Construction

In this work, the volume mesh is generated with the help of the mesh adaptation feature of SC/Tetra. The mesh adaptation feature dynamically adapts the mesh based on flowfield gradients, producing a more refined mesh in areas where larger gradients occur, such as in boundary layers and wakes. The feature was used herein to guide the development of the final meshes used for the results presented herein. The $\alpha = 0°$ case was used for mesh refinement studies. Initially, 1.5 million elements were used to estimate the first solution, and then approximately 250,000–300,000 elements were added successively in regions of gradients noted by the mesh adaptation feature until the total lift and drag forces on the model did not appreciably change. Although the mesh refinement study was conducted on the $\alpha = 0°$ case, each simulation's mesh (10 total) was generated independently on various models where the pitch was prescribed in the CAD software before importing into the CFD preprocessor. However, the same clustering was applied to each model, assuring a similar number of prism elements in boundary layers and similar clustering of tetrahedral elements in boundary regions and wakes. The resulting final meshes contained between 2.6 and 3.2 million elements. Figure 2 presents a cross section of the mesh through the centerline of the $\alpha = 0°$ model; the near-surface prism layers and tetrahedral clustering is typical for all meshes used in this study.

The average surface mesh h ratio, which is the ratio of radii of the inscribed circle and the circumscribed circle of a surface mesh triangle, is between 0.452 and 0.461 for all models. This h ratio describes the quality of surface triangulation, with the best h ratio equal to 0.5 for an equilateral triangle. The tetrahedral volume mesh quality is similarly described by its h ratio, which is the ratio of radii of the inscribed sphere and the circumscribed sphere of a tetrahedral element. The average tetrahedral h ratio is between 0.267 and 0.278 for all models in this study, where a value of 0.333 is the best possible h ratio. These numbers indicate the meshes used for the simulations described herein are of high quality.

Results

Results include comparisons to the experimental data of McBride et al. [4] followed by integrated surface forces on each ribbon. Pressure and vorticity contours, along with selected surface oil-flow visualizations are then presented in order to provide additional insight into the flow behavior around the model. Contours for only a few configurations are shown, and those selected display the typical behavior of the flowfield over all configurations. Results from this

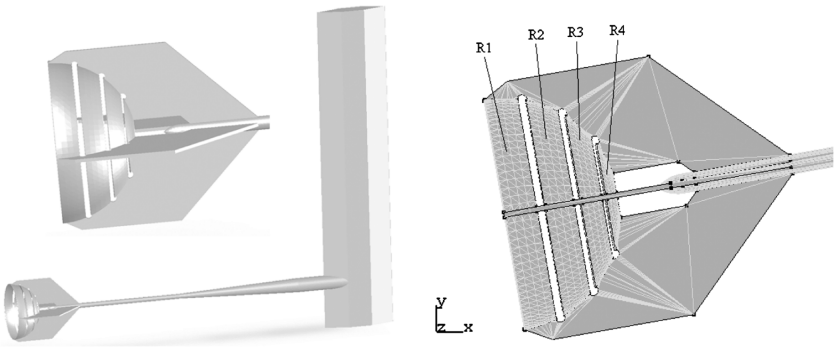

a) Model

b) Coordinate system and ribbon members with -10° pitch model

Fig. 1 Ribbon parachute model and coordinate system.

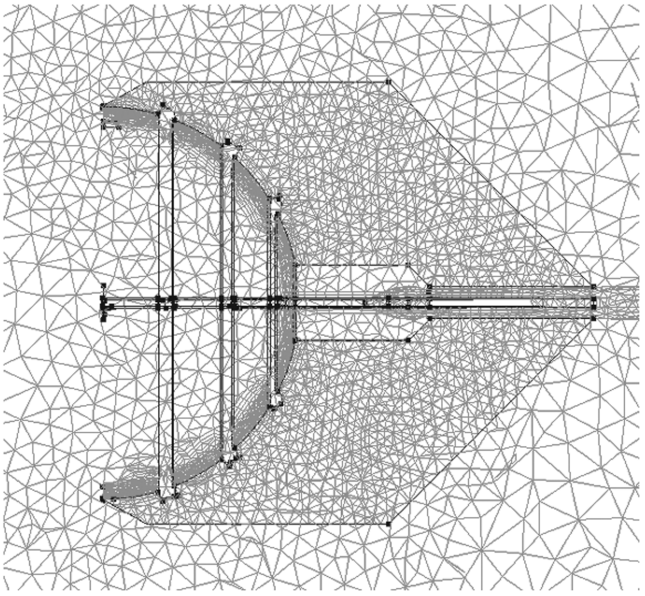

Fig. 2 Typical mesh near ribbons showing boundary elements and tetrahedral clustering ($\alpha = 0°$).

work were originally presented as AIAA paper 2009-3978, while the current article includes results from additional simulations run to include the effects of model roll angle. As such, each pitch angle was simulated twice (one for each roll angle); therefore, the integrated surface forces presented herein are the average value between the two runs. Therefore, there are small differences between results in the current manuscript and in AIAA paper 2009-3978. In addition, contours presented herein are different than the contours presented previously in order to facilitate comparisons to future code validation efforts.

Comparison to Experimental Data

Figure 3 shows three comparisons of the pressure parameter K_p between the current CFD simulations and experimental results across the parachute from the vent ($s/R = 0$) to the skirt ($s/R = 1$); K_p is equal to the difference in static pressure between the inner and outer ribbon surfaces divided by the freestream dynamic pressure. The three comparisons selected, $\alpha = 0$ at $\phi = 0$ in Fig. 3a, $\alpha = -5$ at $\phi = 135$ in Fig. 3b, and $\alpha = -10$ at $\phi = 45$ in Fig. 3c, are typical of all comparisons made to the available data [4] and illustrate the validity of the current simulations. In the experiments, the model was rotated to align the pressure taps to five roll angles, so the model struts were always 45° out of phase with the taps in order to minimize their interference. Thus, the CFD results presented herein contained two simulations for each pitch angle; the first simulation contained the support apparatus with the struts aligned vertically and horizontally, while the second simulation contained a model with the struts oriented diagonally. These two simulations for each pitch angle were necessary to acquire static pressures across the parachute in the locations provided for in the validation data set. In each figure, the number labels in the legend indicate the run numbers from the experimental data set.

Figure 3a ($\alpha = 0$ at $\phi = 0$) shows similar shapes of K_p along the parachute, indicating a good match between the CFD and the experiment. Variations include a smaller pressure difference near the edges of each ribbon and along the length of the first two ribbons encountering the flow (found from 0.83–0.99 s/R and 0.60–0.75 s/R). These trends were typical of all simulations. Figure 3b shows a typical K_p curve for the $\alpha = -5$ simulations, where ribbon 4 near the parachute vent ($s/R = 0$) tends to overpredict the pressure difference peak, while all other ribbons have underpredicted K_p peaks. In general, agreement remains satisfactory. Figure 3c shows the comparison for $\alpha = -10$ at $\phi = 45$, where two modes of behavior were found in the experiments. This figure shows the simulations predicted a pressure difference corresponding to the behavior labeled as mode 1 in the experiments, where K_p is lower for ribbon 4 (vent) and higher for ribbon 3. Taken together, the authors believe these comparisons validate the simulations and resulting discussion presented herein.

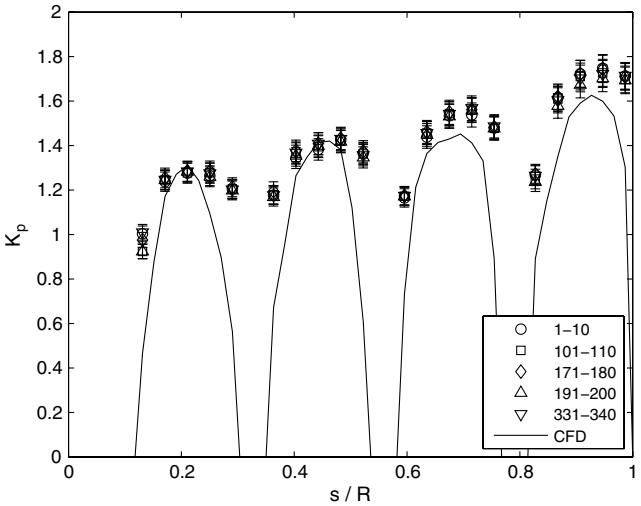

a) α = 0°, ϕ = 0°

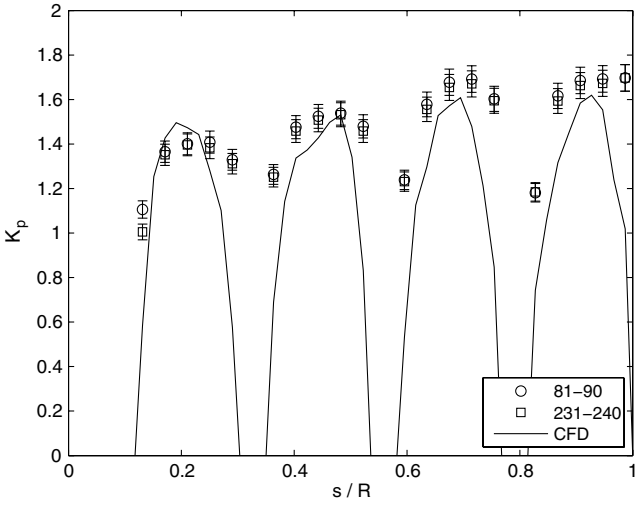

b) α = -5°, ϕ = 135°

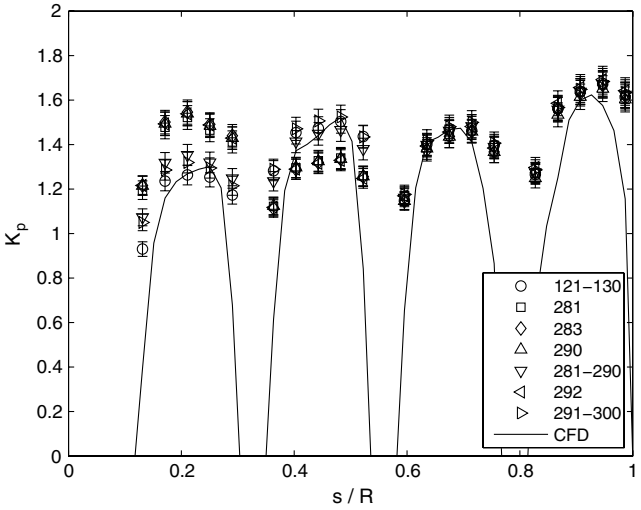

c) α = -10°, ϕ = 45°

Fig. 3 Pressure comparisons with experimental data.

Table 1 Integrated ribbon surface forces, primary pitch angles, N[a]

	$\alpha = 0°$			$\alpha = -5°$			$\alpha = -10°$		
Ribbon	x	y	z	x	y	z	x	y	z
				Pressure					
1	6.76	0.23	0.16	6.54	0.77	−0.12	6.14	0.75	−0.09
2	18.73	0.16	0.11	18.36	2.96	−0.06	17.86	3.78	−0.07
3	20.70	0.09	0.09	20.65	2.51	0.00	19.73	3.13	−0.01
4	10.93	0.03	0.05	11.32	1.03	−0.02	11.06	1.98	0.03
Total	57.12	0.51	0.41	56.87	7.27	−0.20	54.79	9.64	−0.14
				Stress × 100					
1	3.31	0.02	0.05	2.92	−0.18	0.03	2.66	−0.38	0.01
2	0.75	0.00	−0.01	0.83	−0.09	0.00	0.95	−0.28	−0.01
3	0.32	0.02	0.01	0.37	−0.05	−0.01	0.36	−0.26	0.00
4	0.11	0.01	0.00	0.11	−0.03	0.00	0.14	−0.09	0.02
Total	4.49	0.06	0.05	4.23	−0.35	0.02	4.11	−1.01	0.02

[a]Averaged over simulations having model mounts in both orientations.

Table 2 Integrated ribbon surface forces, secondary pitch angles, N[a]

	$\alpha = -8°$						$\alpha = -12°$					
	Pressure			Stress × 100			Pressure			Stress × 100		
Ribbon	x	y	z	x	y	y	x	y	z	x	y	z
1	6.30	0.83	−0.09	2.85	−0.30	0.04	6.01	0.78	0.02	2.73	−0.40	0.00
2	18.01	3.43	−0.05	0.92	−0.23	0.01	18.13	4.16	−0.01	0.94	−0.33	−0.02
3	20.02	3.01	0.01	0.37	−0.12	0.01	19.83	3.47	−0.04	0.46	−0.24	−0.02
4	11.26	1.52	0.00	0.13	−0.06	0.00	10.78	2.41	0.01	0.17	−0.09	−0.01
Total	55.59	8.79	−0.13	4.27	−0.71	0.06	54.75	10.82	−0.02	4.30	−1.06	−0.05

[a]Averaged over simulations having model mounts in both orientations.

Integrated Ribbon Surface Forces

Table 1 presents the integrated surface pressure and tangential stress forces for the primary pitch angles of 0, −5, and −10°. These pitch angles match those in the experiments of McBride et al. [4]. Table 2 presents the integrated surface forces for the secondary pitch angles of −8 and −12°. These angles were simulated in order to look for occurrences of the bimodal pressure behavior found in the experiments. However, only the first mode was found, as described previously. The integrated forces are included here as secondary angles to provide additional validation data. As noted previously, the forces presented are the average values between the two simulated roll angles.

The surface forces seen in Table 1 show several trends. First, the pressure drag in the x direction reaches a maximum on ribbon 3 for each angle of attack. Ribbon 1 has the least amount of pressure drag, ribbon 2 has the second highest, and ribbon 4 has the second lowest. In general, a more negative pitch angle causes the total pressure drag to decrease. With decreasing α, the pressure drag decreases on ribbons 1, 2, and 3 but increases on ribbon 4 until after $\alpha = -5$ where it follows the trend. Aside from a pitch angle of 0°, ribbon 2 experiences the highest pressure in the y direction and ribbon 1 experiences the least. The 0° pitch angle experiences negligible pressure in the y and z directions because the model is parallel to the x axis so that pressure forces in the other directions cancel due to symmetry. As the pitch angle decreases, however, the pressure distribution shifts and pressure in the y direction becomes significant. In general, decreasing the pitch angle increases the total pressure in the y direction away from the pitch direction. Ribbons 2 through 4 see a steady increase in y-direction pressure with more negative α, with ribbon 2 holding the greatest y-direction pressure. The pressure in the z direction for each pitch angle remains small, since all models are symmetric about that axis. The forces displayed in Table 2 illustrate similar trends for $\alpha = -8$ and −12°.

In the x direction, the skin friction drag is at a maximum on ribbon 1 for each pitch angle and then decreases on each successive ribbon, so that on ribbon 4, it is nearly negligible. Except for $\alpha = 0°$, the skin friction force in the y direction follows the same trend, except all the values are negative, indicating surface stress force pulling the parachute toward the pitch angle. The magnitude of this surface stress increases with an increase in pitch angle. Again, in the z direction, the values are so small that they can be considered negligible due to symmetry.

Flowfield Contours

Line contours of pressure coefficient (C_p) and vorticity magnitude are presented for pitch angles of 0, −5, and −10° in Figs. 4 and 5, respectively. Here, pressure coefficient is defined as the static pressure minus the freestream static pressure and divided by the freestream dynamic pressure. For all pressure coefficient contours, the maximum contour value is 1.0 and the minimum value is −2.0 with a step of 0.075, and all vorticity contours have a maximum value of 250 s^{-1} and a minimum of 0 with a step of 16.67. These figures show comparisons among pitch angles of 0, −5, and −10° at the vertical roll angles of 0 and 180°, and at the diagonal roll angles of 45 and 225°.

Figure 4a shows C_p for the vertical plane, where the roll angle ϕ is 0° at the bottom of the figure and 180° at the top of the figure. As can be seen, the pitch angle of 0° results in a symmetric pressure distribution. As noted in Table 1, the pressure is greatest on ribbons 2 and 3. The areas of high pressure start on the inside surface perimeter and work toward the center in both the upper and lower sections of the parachute. Slightly less pressure is observed in the opening of the parachute, and negative pressure can be seen along the outer edges. Pressure recovery on the outer surfaces occurs near the middle of ribbon 1, and this location shifts slightly toward the ribbon leading edges for ribbons 2, 3, and 4. Comparing to $\phi = 45°$ (bottom) and $\phi = 225°$ (top) in Fig. 4b, there is a slightly larger area of higher pressure in the region immediately upstream of the vent. The reader is reminded that results for $\phi = 45$ and 225° were generated from simulations containing the geometry (and model struts) at a roll angle 45° out of phase compared with the results presented for $\alpha = 0$ and 180°. This leads to a different interaction with the test section boundaries, which could cause slight differences in the contour locations. In this region, the CFD predicts a maximum pressure coefficient value of 1.02, a value that is questionable for subsonic

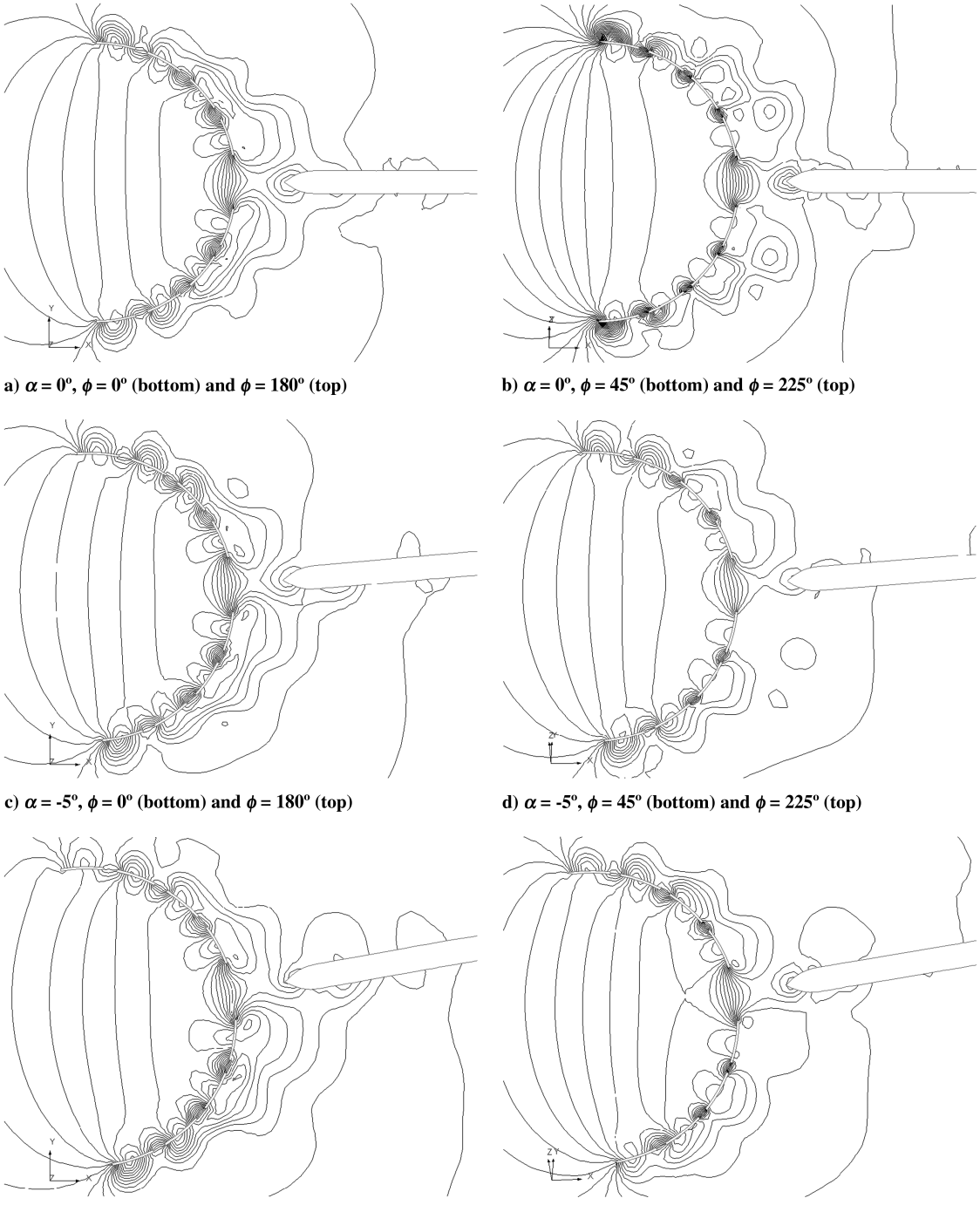

a) $\alpha = 0^o$, $\phi = 0^o$ (bottom) and $\phi = 180^o$ (top)

b) $\alpha = 0^o$, $\phi = 45^o$ (bottom) and $\phi = 225^o$ (top)

c) $\alpha = -5^o$, $\phi = 0^o$ (bottom) and $\phi = 180^o$ (top)

d) $\alpha = -5^o$, $\phi = 45^o$ (bottom) and $\phi = 225^o$ (top)

e) $\alpha = -10^o$, $\phi = 0^o$ (bottom) and $\phi = 180^o$ (top)

f) $\alpha = -10^o$, $\phi = 45^o$ (bottom) and $\phi = 225^o$ (top)

Fig. 4 Pressure coefficient contours (maximum value is 1.0; minimum value is −2.0; step of 0.075).

flows. Batchelor notes that local total pressures can exceed the freestream total pressures in highly viscous flows due to the viscous work in stagnation regions [8]. However, the authors believe it is more likely that the k-ϵ turbulence model in the RANS simulations is to blame, causing an overprediction of pressure through the eddy viscosity in the stagnation regions near the ribbons that leads to the rise in pressure coefficient over one. In addition, the low-pressure regions on the downstream side of the ribbons in Fig. 4b exhibit minimum C_p values near −1.94, while those of Fig. 4a show minimum C_p values near −1.85. Thus, the simulations for the 45 and 225° roll angle results, which contain the model struts at the 0, 90, 180, and 270° roll angles, have larger maximums and lower minimums than their counterparts containing the model struts at the diagonal positions. This is also reflected with the higher number of contour lines seen in the figures.

Figures 4c and 4d for the pitch angle of −5° show how decreasing the pitch angle causes the high-pressure areas to shift toward the lower part of the parachute. High pressure can still be observed on the upper half of the parachute on the perimeter, predominantly on the leading edge of each ribbon. In the lower half, the high pressure is still centered around ribbons 2 and 3, and slightly less pressure is observed in the majority of the parachute. Pressure recovery locations on the outer surfaces on the top ribbon sections move slightly upstream with decreasing pitch angle, while locations on the bottom surfaces move slightly downstream. The lower-pressure regions immediately downstream of the ribbons also extend further downstream for the lower half of the model. This was also expected, as the model supports tilt toward the upper half, blocking the wake path. Figures 4e and 4f for the pitch angle of −10° again show the shift in higher-pressure regions toward the

pitch direction and larger wake regions behind the downstream ribbon faces.

Figure 5 shows the complex interactions of boundary and detached shear layers among the ribbons with line contours of vorticity magnitude. Figure 5a shows the vertical plane containing $\phi = 0$ (bottom) and $\phi = 180$ (top) for zero pitch angle, while Fig. 5b shows the diagonal plane containing $\phi = 45$ (bottom) and $\phi = 225$ (top) at zero pitch. In general, these two figures illustrate a symmetric vorticity pattern, where negative spanwise vorticity generated on the top of ribbon surfaces is matched by positive spanwise vorticity generated on the bottom of ribbon surfaces, resulting in the same magnitude of total vorticity when compared across the hemisphere. The sizes of the local vorticity regions near ribbon surfaces correspond to the size of the boundary layers and the degree of mixing occurring in the detached shear layers emanating from each inner and outer surface. Figure 5a, showing roll angles of 0 and 180° for zero pitch, illustrates the curling of flow around each ribbon edge, which creates a large wake downstream of each ribbon section. Vorticity is generated upstream of the ribbon 1 leading edges, where a laminar separation is noticed on both inner and outer surfaces for zero pitch angle. The inner side experiences a turbulent reattachment near 60–70% of the ribbon length, depending on orientation of the model struts (Figs. 5a or 5b). The quick growth of vorticity near the middle of the inner surfaces of ribbon 1 is caused by a significant growth in turbulent energy upstream of the reattachment locations. Thick boundary layers are then quickly generated, illustrating the highly

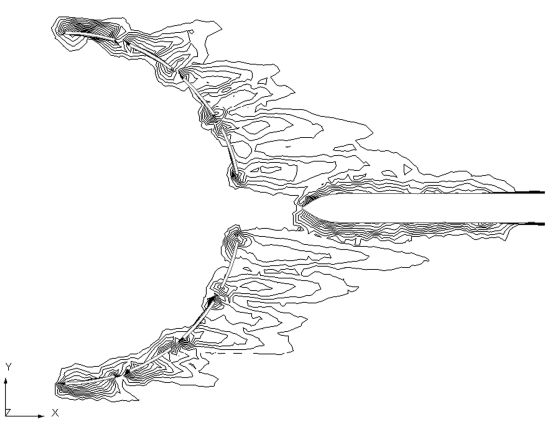

a) $\alpha = 0^o$, $\phi = 0^o$ (bottom) and $\phi = 180^o$ (top)

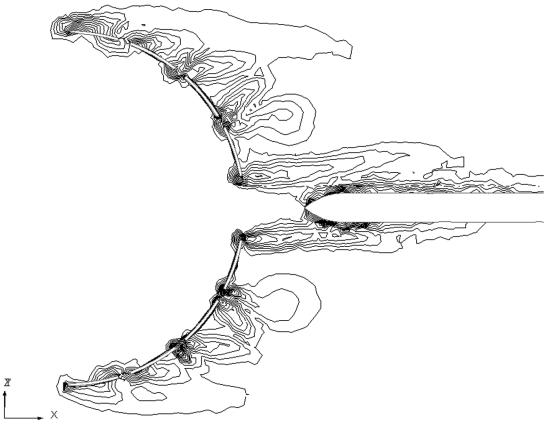

b) $\alpha = 0^o$, $\phi = 45^o$ (bottom) and $\phi = 225^o$ (top)

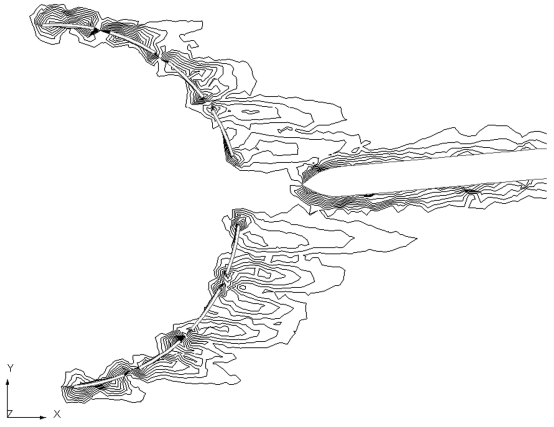

c) $\alpha = -5^o$, $\phi = 0^o$ (bottom) and $\phi = 180^o$ (top)

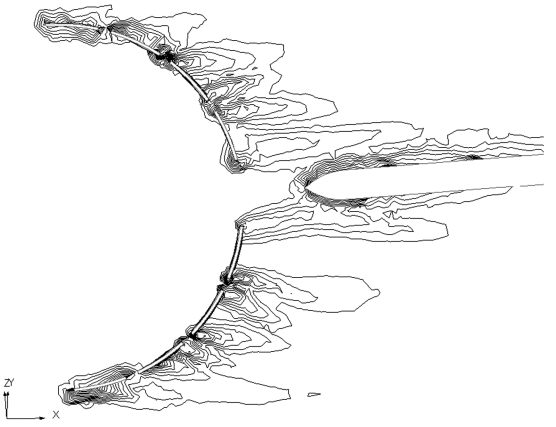

d) $\alpha = -5^o$, $\phi = 45^o$ (bottom) and $\phi = 225^o$ (top)

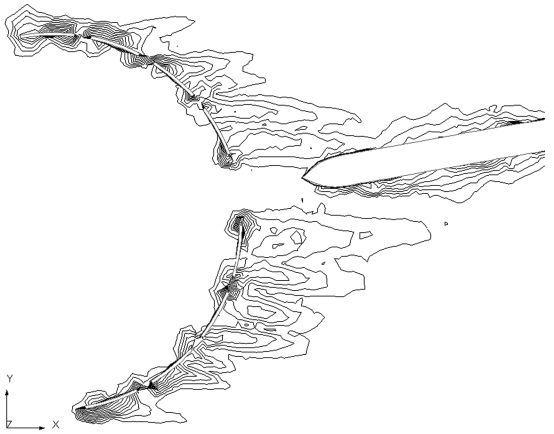

e) $\alpha = -10^o$, $\phi = 0^o$ (bottom) and $\phi = 180^o$ (top)

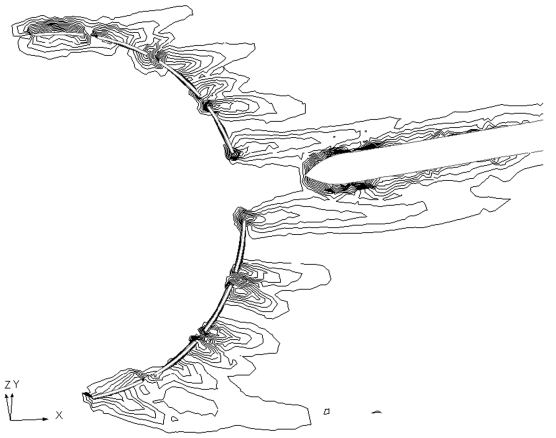

f) $\alpha = -10^o$, $\phi = 45^o$ (bottom) and $\phi = 225^o$ (top)

Fig. 5 Vorticity magnitude contours [s^1] (maximum value is 250; minimum value is 0; step of 16.67).

unsteady nature of the flowfield inside the ribbon parachute geometry. As pitch angle decreases to −8° and below, the inner ribbon 1 reattachment line proceeds further downstream. The outer sides of ribbon 1 at zero pitch separate near the leading edges for both model strut orientations and reattach further downstream near 15–20% of the surface length. This generates a large amount of vorticity that continues to extend away from the ribbon surfaces. This boundary-layer vorticity sheds downstream, significantly affecting the flow encountering ribbon 2. As pitch angle is decreased to −5°, the shed vorticity patterns become asymmetric about the model's axis of symmetry. The inner ribbon 1 reattachment locations remain relatively unchanged for $\phi = 0$ and 180°, while the outer reattachment locations shift slightly upstream for $\phi = 180°$ and slightly downstream for $\phi = 0°$. This trend is different for the inner ribbon surfaces for the 45 and 225° roll angles seen in Fig. 5d, where the inner ribbon 1 reattachment locations shift further downstream. Decreasing pitch angle further to −10° in Figs. 5e and 5f reveals similar trends for ribbon 1.

The vorticity shed downstream from ribbon 1 merges with the vorticity generated on the leading edges and surfaces of ribbon 2. As the outer and inner surfaces of ribbons 1 and 2 are more aligned than any other ribbon pairs, it is understandable that the adjacent boundary and detached shear layers sharing the same-sign vorticity could merge and produce larger vortical regions. This trend suggests that the gap between ribbons 1 and 2 is not large enough to share their boundary layers to a high enough degree to cancel out the opposing-sign vorticity. This combining and enlarging trend is noticed at all pitch angles, with two noticeable differences. First, the negative y-direction distance of positive vortical activity is located farther away from the model centerline with decreasing pitch. The second consistent difference is the positive y direction; outer vortical regions of negative vorticity also shrink in region size with decreasing pitch angle.

Moving downstream to the trailing edges of ribbon 3 shows a different trend. Here, the surface geometry contains more curvature and therefore spreads the developing inner- and outer-surface boundary layers further apart before shedding into the gap between ribbons 3 and 4. As a consequence, at $\alpha = 0°$, the regions of same-sign outer-surface vorticity that joined between ribbons 1 and 2 are now separated by a thin region of opposing-sign vorticity, which appears to come from the inner side boundary layer of ribbon 1; since $\alpha = 0°$, the same is true all around the parachute. Decreasing the pitch changes the result, since the positive y-direction region shows no noticeable region of opposing-sign vorticity between the shear layers created from the inner surface of ribbons 1 and 2. In the region below the model (negative y direction), a patch of opposing-sign vorticity does exist between the positive vorticity generated on the outer surfaces of ribbons 1 and 2. The authors believe this is again due to the extra room caused by the pitch angle in the bottom wakes before interaction with the opposing-sign vorticity generated on the adjacent surfaces.

The behavior noticed at the downstream edge of ribbon 3 is very similar to the behavior at the downstream edge of ribbon 4 for all pitch angles. However, at zero pitch, the small patch of opposing-sign vorticity, which was previously located between the vorticity generated on the outer surfaces of ribbons 1 and 2, has disappeared. This signifies that by the downstream edge of ribbon 4, the outermost vorticity in the upper quadrants (positive y direction), is dominated by the outer surfaces of the preceding ribbons. Closer to the model axis, the region of positive vorticity generated on the inner surface of ribbon 3 grows larger, while smaller patches of positive and negative vorticity develop on the inner and outer surfaces of ribbon 4, respectively. For all negative pitch angles, progressing into the lower quadrants (negative y direction) reveal a different vorticity composition than the upper quadrants (again, as a direct result from the model's pitch angle). Here, the outermost vorticity is dominated by the outer surface of ribbon 1, while a small patch of vorticity generated on the inner surface of ribbon 1 remains between the opposing, positive vorticity from the outer surface of ribbon 2. Thus, the vorticity generated on the inner surfaces of ribbons 1 and 2 remains visible by the downstream edge of ribbon 4.

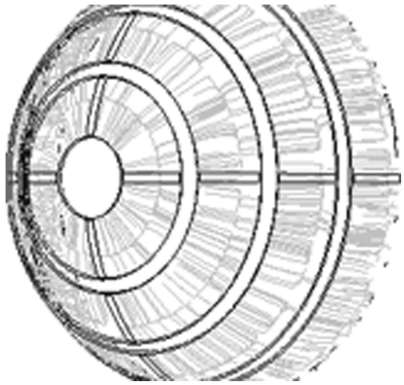

Fig. 6 Oil-flow pattern on outer surface at zero pitch (flow from right to left).

Surface Oil-Flow Patterns

To provide a better understanding of the flow physics occurring in and around the ribbon parachute model, computational oil-flow visualizations were analyzed on the ribbon surfaces. Oil-flow visualizations provide surface shear patterns on the ribbons that can highlight critical locations such as separation, reattachment, or impingement lines and foci. These details can give a greater understanding of the flow around a surface; interpretations provided herein are based upon the guidelines described by Tobak and Peake [9].

Figure 6 shows an example of these oil-flow visualizations for the outer surfaces at zero pitch, where the flow is going from the right to the left. According to Tobak and Peake [9], the lines just downstream of the leading edges indicate reattachment lines, since the surface vectors are diverging away from the line. Because only reattachment lines are seen in this figure, this indicates that the flows on the outer surfaces separate from the leading edges. Ribbon 1 quickly reattaches in the first 15% of the outer ribbon length. Successive ribbons experience a downstream progression of reattachment location: from near 15% on ribbon 1 to 35–40% on the outer surface of ribbon 4. As pitch angle is decreased, the pattern remains nearly the same, with minimal downstream progression of reattachment locations. However, at $\alpha = -12°$, there is a pronounced difference in reattachment behavior, where the reattachment line on all ribbons shows longer separation bubbles that reattach further downstream than previous pitch angles. The outer-surface oil-flow results in this figure also show reattachment foci near the model struts, showing the effects of the struts in causing added swirling in the local flowfields; similar behavior in reattachment foci was observed in the inner ribbon surfaces near the struts.

Conclusions

In this paper, a RANS flow solver with the k-ϵ turbulence model was used to simulate the steady-state flow around a ribbon parachute model at five pitch angles and two model support roll angles. Comparisons of pressure coefficient with experimental data confirm the accuracy of the simulations. Results show the pressure drag is greatest on ribbons 2 and 3, with ribbon 3 holding the greatest pressure drag for all pitch angles. Ribbon 1 creates the least amount of pressure drag, followed by ribbon 4, with the second lowest pressure drag. The total pressure drag decreases with decreasing pitch angle. Pressure coefficient contours illustrated the regions of pressure buildup and wake development.

Vorticity magnitude contours also illustrated the regions of wake development, as well as the interaction of boundary-layer developments among the four ribbons and slots in between. These contours showed that the boundary-layer vorticity created on each ribbon's inner and outer surfaces mixed with same-sign and opposite-sign vorticity patches from adjacent ribbons with downstream progression. It appears the vorticity generated from ribbon 1 constructively adds to the vorticity generated from ribbon 2 for all pitch angles,

since the two ribbons are geometrically aligned, more so than any other adjacent ribbon pair. By ribbon 3, the model's curvature has influenced the spreading of vorticity affecting the top and bottom quadrants differently, with the bottom quadrants having more space between boundary and detached shear layers due to the pitch angle. This causes more mixing of boundary layers in the top quadrants while the bottom quadrants' opposing-sign vorticity patches remain in that state further downstream than the upper quadrants' boundary layers.

Computational oil-flow visualizations also provided insight into the separation and reattachment locations for both the inner and outer ribbon surfaces. The ribbon 1 reattachment line moves downstream with decreasing pitch angle, while successive ribbons exhibit more upstream reattachment lines on the inner surface, meaning the separation bubbles become shorter with downstream progression. On the outer surfaces, successive ribbons exhibit a downstream progression of reattachment locations, contrary to the inner surfaces. At $\alpha = -12^\circ$, there is a pronounced lengthening of the separation bubbles on all four ribbons, which may indicate bursting of the outer-surface separation bubbles. These separations, on each ribbon surface, help generate the large degree of unsteadiness seen in the vorticity results.

These results collectively provide a comprehensive data set based on a well-documented experimental setup that can be used for future validation of the CFD component during FSI code development.

Acknowledgments

The authors wish to thank Jean Potvin of Saint Louis University for helpful discussion during this project's development. We would also like to thank David Welsh of Cradle North America and Sunil Vytla of Wright State University for helpful discussions regarding CAD model preparation for computational fluid dynamics analysis and Sally Warning for her assistance preparing figures.

References

[1] Seeger, M., Müller, L., Carlsson, P., Bury, Y., Pressigny, Y., Lallemand, G., Vallance, M., Wheeler, R., Benney, R., Charles, R., Morton, S., and Tavan, S., "Four-Powers Long Term Technology Projects: 'Airflow Influence on Airdrop' and '2nd Precision Airdrop Improvements'," AIAA Paper 2005-1602, 2005.

[2] Strickland, J., and Higuchi, H., "Parachute Aerodynamics: An Assessment of Prediction Capability," *Journal of Aircraft*, Vol. 33, No. 2, 1996, pp. 241–252. doi:10.2514/3.46930

[3] *AIAA Guide for the Verification and Validation of Computational Fluid Dynamics Simulations*, AIAA Standards Series, G-077-1998e, AIAA, Reston, VA, 1998.

[4] McBride, D., Henfling, J., and Clark, E. "Pressure Data for the Experimental Validation of a Vortex-Based Parachute Inflation Code," AIAA Paper 1999-1747, 1999.

[5] Patanker, S., *Numerical Heat Transfer and Fluid Flow*, Hemisphere, New York, 1980.

[6] van Leer, B., "Towards the Ultimate Conservation Difference Scheme 4: A New Approach to Numerical Convection," *Journal of Computational Physics*, Vol. 23, No. 3, 1977, pp. 276–299. doi:10.1016/0021-9991(77)90095-X

[7] Rhie, C., and Chow, W., "Numerical Study of the Turbulent Flow Past an Airfoil with Trailing Edge Separation," *AIAA Journal*, Vol. 21, No. 11, 1983, pp. 1525–1532. doi:10.2514/3.8284

[8] Batchelor, G. K., *An Introduction to Fluid Dynamics*, Cambridge Univ. Press, Cambridge, England, U.K., 2000.

[9] Tobak, M., and Peake, D. "Topology of Three-Dimensional Separated Flows," *Annual Review of Fluid Mechanics*, Vol. 14, No. 1, 1982, pp. 61–85. doi:10.1146/annurev.fl.14.010182.000425